Ductile crystalline–amorphous nanolaminates

Yinmin Wang*[†‡], Ju Li[§], Alex V. Hamza*[†], and Troy W. Barbee, Jr.[†]

*Nanoscale Synthesis and Characterization Laboratory, [†]Chemistry, Materials, and Life Sciences Directorate, Lawrence Livermore National Laboratory, Livermore, CA 94550; and [§]Department of Materials Science and Engineering, Ohio State University, Columbus, OH 43210

Edited by William D. Nix, Stanford University, Stanford, CA, and approved May 25, 2007 (received for review March 14, 2007)

It is known that the room-temperature plastic deformation of bulk metallic glasses is compromised by strain softening and shear localization, resulting in near-zero tensile ductility. The incorporation of metallic glasses into engineering materials, therefore, is often accompanied by complete brittleness or an apparent loss of useful tensile ductility. Here we report the observation of an exceptional tensile ductility in crystalline copper/copper–zirconium glass nanolaminates. These nanocrystalline–amorphous nanolaminates exhibit a high flow stress of 1.09 ± 0.02 GPa, a nearly elastic-perfectly plastic behavior without necking, and a tensile elongation to failure of 13.8 ± 1.7%, which is six to eight times higher than that typically observed in conventional crystalline–crystalline nanolaminates (<2%) and most other nanocrystalline materials. Transmission electron microscopy and atomistic simulations demonstrate that shear banding instability no longer afflicts the 5- to 10-nm-thick nanolaminate glassy layers during tensile deformation, which also act as high-capacity sinks for dislocations, enabling absorption of free volume and free energy transported by the dislocations; the amorphous–crystal interfaces exhibit unique inelastic shear (slip) transfer characteristics, fundamentally different from those of grain boundaries. Nanoscale metallic glass layers therefore may offer great benefits in engineering the plasticity of crystalline materials and opening new avenues for improving their strength and ductility.

metallic glass | size-dependent plasticity | nanocrystalline materials | amorphous–crystalline interface | tensile ductility

A traditional strategy to develop ultrahigh-strength crystalline materials is to limit or inhibit the motion of dislocations required for plastic deformation (1–3) so that a higher applied stress is necessary. Examples of such advanced materials include thin films (4), nanocrystalline metals (5–7), and nanolaminates (8–10). As dislocation motion in high-strength crystalline materials becomes increasingly difficult (11), the ductility, i.e., the ability of a material to change shape without catastrophic failure, is often reduced dramatically (6, 7). In bulk metallic glasses, plastic deformation is not enabled by dislocations (12–21) but rather by clusters of atoms that undergo cooperative shear displacements [shear transformation zones (STZs)] (16); in the extreme limit of homogeneous-to-inhomogeneous flow transition, shear bands of nanoscale width form (17, 19–21). The formation of such shear bands causes large strain softening and abrupt rupture of the metallic glasses. By way of contrast, large compressive plastic strains have been obtained in several bulk metallic glasses (12–14). Nonetheless, they show near-zero macroscopic ductility when subjected to tensile loading. To our knowledge, there is no experimental evidence currently suggesting that macroscopic metallic glass samples can sustain large tensile plasticity. An interesting question arises whether shear banding remains the Achilles' heel of metallic glasses as their dimensions approach the nanoscale.

The nanocrystalline Cu and nanoscale Cu/Zr glass nanolaminate samples were fabricated by magnetron sputter deposition of alternating layers of Cu and Zr. A solid-state amorphization reaction between the Cu and Zr layers resulted in the formation of the nanolayer Cu/Zr metallic glass. The cross-sectional transmission electron microscopy (TEM) image in Fig. 1*A* shows that the as-fabricated nanolaminate foils consist of well defined, alternating layers of Cu nanocrystals and Cu/Zr metallic glass. The average grain size of nanocrystalline copper (≈35 nm) is approximately equal to the crystal layer thickness (this is confirmed through the plan-view TEM image shown in Fig. 1*B*), whereas the thickness of the metallic glass layers (≈5–10 nm) is controlled by the deposition thickness of elemental Zr (5 nm of amorphous $Cu_{\approx 3}Zr$ forms from 2.5 nm of Zr and 3.8 nm of Cu). High-resolution TEM examination shows that the nanocrystalline Cu grains/layers are nearly dislocation-free, with a {111} out-of-plane texture and little evidence of growth twins. Electron dispersive x-ray spectrometry suggests that the metallic glass layer has a composition of $Cu_{\approx 3}Zr$, in agreement with the atomic ratio defined by the Zr and Cu layer thickness forming these layers.

Room-temperature uniaxial tensile tests of 5/35 (i.e., a 5-nm-thick $Cu_{\approx 3}Zr$ metallic glass layer and a 35-nm-thick nanocrystalline Cu layer; the same notation applies throughout the text) samples at a strain rate of 1×10^{-4} s^{-1} reveal that the nanolaminate exhibits a high strength (Fig. 1*C*) with the steady-state flow stress of 1,090 ± 20 MPa. In contrast, the flow stress of crystalline Cu layers with the thickness of 35 nm is estimated to be 630 MPa (22), and single-phase bulk nanocrystalline Cu with an average grain size of 30 nm has a tensile strength of <800 MPa (one example is shown in Fig. 1*C*) (23). These strengths are significantly less than that of this nanocrystalline–amorphous nanolaminate, indicating that the addition of amorphous layers has considerably elevated the strength of otherwise nanocrystalline copper layers. The 5/35 nanolaminate also shows a large tensile ductility, with an elongation to failure (ε%) of 13.8 ± 1.7%. Replacing the amorphous metallic glass layers with other layers of crystalline phase, such as 304 stainless steel or Nb (e.g., Cu/304 SS or Cu/Nb nanolaminates), leads to a low ductility, with an ε% of <2% (Fig. 1*C*) (8–10). This sharp decrease in ductility is the major limitation encountered in all high-strength crystalline–crystalline multilayer materials with nanometer-sized bilayers ($\lambda \leq 40$ nm) (8, 10), as well as in many single-phase nanocrystalline metals with unimodal grain size distributions (Fig. 1*C*, nanocrystalline Cu curve) (6, 23). It is worth pointing out that high-strength and high-ductility nanostructured copper has been reported before (see, for example, refs. 24 and 25). However, the observed tensile ductility of the nanocrystalline Cu–amorphous $Cu_{\approx 3}Zr$ nanolaminate is unexpected in view of the near-zero tensile ductility of bulk metallic glasses as well as the characteristically low ductility in nanoscale microstructure materials.

Another striking feature of nanocrystalline–amorphous nanolaminates (Fig. 1*C*) is that essentially zero strain hardening occurs during plastic deformation, indicative of an elastic-perfectly plastic

Author contributions: Y.W., J.L., and T.W.B. designed research; Y.W., J.L., and T.W.B. performed research; Y.W., J.L., and T.W.B. analyzed data; and Y.W., J.L., A.V.H., and T.W.B. wrote the paper.

The authors declare no conflict of interest.

This article is a PNAS Direct Submission.

Freely available online through the PNAS open access option.

Abbreviations: ACI, amorphous–crystalline interface; GB, grain boundary; MD, molecular dynamics; STZ, shear transformation zone; TEM, transmission electron microscopy.

[‡]To whom correspondence should be addressed. E-mail: ymwang@llnl.gov.

This article contains supporting information online at www.pnas.org/cgi/content/full/0702344104/DC1.

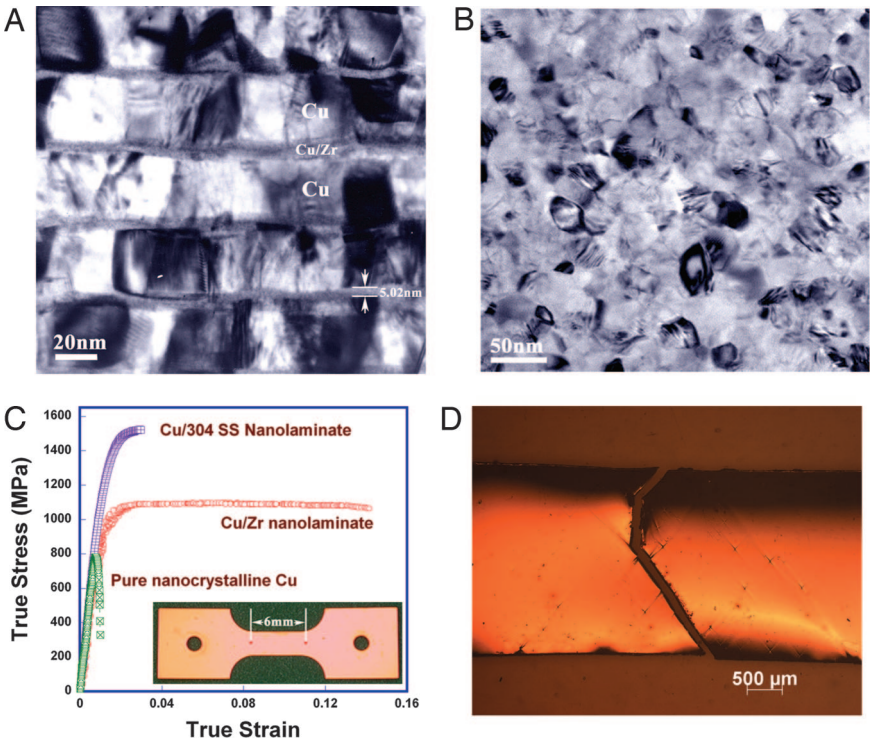

Fig. 1. Microstructures and tensile properties of Cu/Zr nanolaminates. (*A* and *B*) Cross-sectional (*A*) and plan-view (*B*) TEM images of the as-deposited 5/35 nanocrystalline Cu and amorphous Cu/Zr intermixing multilayer nanostructures. The average grain size in the nanocrystalline layers is approximately equal to the individual layer thickness. (*C*) Room-temperature tensile true stress–strain curves of the nanocrystalline–amorphous nanolaminate at the strain rate of 1×10^{-4} s^{-1}, in comparison with those of Cu/304 stainless steel crystalline multilayer with an individual layer thickness of 25 nm and pure nanocrystalline Cu with an average grain size of ≈30 nm. The curve for pure nanocrystalline Cu is an engineering stress–strain plot taken from ref. 23. The Cu/Zr nanolaminate has an average tensile elongation to failure of 13.8 ± 1.7% and a steady-state flow stress of 1,090 ± 20 MPa, in contrast with the low ductility (<2%) seen in conventional crystalline nanolaminates (Cu/304 SS) and pure nanocrystalline Cu. In addition, the nanoscale metallic-glass modulated nanolaminates exhibit a near-perfect plastic flow behavior without necking. (*D*) The top-view of the gauge section after fracture for 5/35 Cu/Zu nanolaminate.

behavior without neck formation. Such near-perfect elastoplasticity in tension is quite unusual and has only been observed in pure nanocrystalline copper (5) when deformed at the extremely slow strain rate of 5×10^{-6} s^{-1}. The physical mechanism of this behavior in the pure nanocrystalline copper was related to a grain boundary (GB) sliding mechanism (7), which often leads to a drop of the flow stress (7, 26). The high flow stress (~1.09 GPa) and the near-perfectly plastic flow behavior observed in our samples at room temperature and at a much higher strain rate of 10^{-4} s^{-1} are inconsistent with the observations in pure nanocrystalline materials, indicating an alternative deformation mechanism. The nearly perfect plasticity observed here is in apparent contradiction with the Considère criterion, which predicts the mathematical onset of necking when $d\sigma/d\varepsilon \leq \sigma$ is reached, at constant strain rate, $\dot{\varepsilon}$. For a thin sheet sample tested in tension, the criterion for geometrical softening via localized necking is $d\sigma/d\varepsilon < \sigma/2$ (27). Neither criterion, however, predicts the rate of necking leading to discernable shape change and ultimate failure. According to Hutchinson and Neale's (28) nonlinear analysis for strain-rate-sensitive materials, one can expect a substantial range of near-uniform straining before necking failure provided that the strain rate sensitivity (m) of the material is in the intermediate range of a few percent. We have therefore carried out the strain rate jump tests of the 5/35 Cu/Zr nanolaminates, which reveal a strain rate sensitivity (m) value of 0.03 in the strain rate range used in our experiments (1.0×10^{-4} to 7.0×10^{-4} s^{-1}). This represents a 5-fold increase over the m value of 0.006 for conventional coarse-grained Cu (29, 30). This m value is large enough to render ≈10% near-uniform tensile elongation, following Hutchinson and Neale's analysis (28). In our experiments, localized deformation was not visually detected before the tensile strain reached ≈10–11%. However, necking eventually set in beyond this strain. Note in Fig. 1*D* that the gauge-width variation is <0.9% along the gauge-length direction after fracture and that the 5/35 nanolaminate samples ultimately failed along narrow bands inclined at an angle of ≈55° with respect to the tensile axis, coincident with the necking direction predicted for thin sheet samples by McClintock and Argon (27).

To understand the physical origin of large tensile ductility and near perfectly plastic flow behavior of the nanolaminates, we examined by high-resolution TEM the microstructures of nanolaminate foils at different tensile strains (Fig. 2 *A–D*). Heavy dislocation storage or pileup was not revealed in the deformed nanocrystalline layers except for a few deformation twins (pointed with arrows in Fig. 2*E*), one end of which tends to terminate at the amorphous–crystalline interfaces (ACIs) or the copper–copper GBs. This implies that, in addition to GBs, the ACIs may have become the sources for dislocation nucleation. Deformation twinning during tensile testing of nanocrystalline copper at room-temperature and quasistatic strain rates is quite rare, indicative of high stress levels achieved in the nanograins. The formation of deformation twins leads to a minuscule strain hardening effect in the nanocrystalline layers and may help to balance potential shear softening in the amorphous layers, rendering an overall near-zero strain hardening behavior seen in Fig. 1*C*. Because of the comparable areal density of ACIs and copper–copper GBs, we hypothesize that the ACIs play a significant role (as the GB mechanisms) (10, 21) in enhancing both the ductility and the m value of our samples.

High-resolution TEM observations of uniaxial tensile-deformed nanolaminates show that the nanoscale (5–10 nm) amorphous layers do not exhibit shear bands or nanocracks, even when the local tensile strains reach as high as ≈14% (this value is deduced from the thickness reduction of the amorphous layer by comparing Fig. 1*A* and Fig. 2*E*, assuming a constant volume condition in plastic deformation), indicative of homogeneous flow in the metallic glass layers. This nanoscale tensile ductility in the amorphous layers is notable, considering that bulk metallic glasses exhibit essentially zero ductility in tension. Our room-temperature rolling experiments further indicate that the plastic flow of the nanoscale metallic glass layers remains uniform, even when the individual layer thickness reduction is 50%. The lack of shear banding in the nanoscale metallic glass layers may be understood in terms of the aged-rejuvenation-glue-liquid shear band model (18). It predicts that the size of the stressed metallic glass region must exceed an

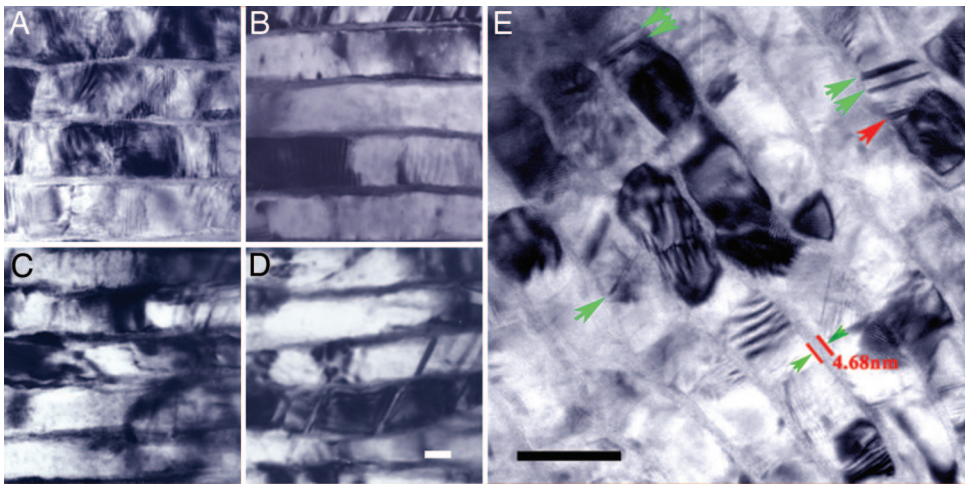

Fig. 2. Deformation microstructures. (*A–D*) Sequential TEM images of the 5/35 Cu/Zr nanolaminate at tensile strains of 0% (*A*), 2% (*B*), 7% (*C*), and 10% (*D*). The gradual reductions of individual nanocrystalline and nanoscale amorphous layers can be seen with increasing strains. Some deformation twins are discernable, but dislocation pileup is not observed at any strains. (*E*) A high-resolution TEM image of 5/35 Cu/Zr nanolaminate after fracture. Deformation twins can be seen inside several nanograins, two ends of which tend to terminate at the ACIs (green arrows) or at the GBs (red arrow), suggesting that the ACIs may have become the dislocation nucleation sources. Stacking faults are also seen at high-resolution TEM. (Scale bars: *A–D*, 20 nm; *E*, 50 nm.)

incubation length scale L_{inc} in order for STZs to develop into mature shear bands:

$$L_{\text{inc}} = \frac{\alpha c_v^2 (T_g - T_{\text{env}})^2}{\tau_{\text{glue}}{}^2 c_s}, \qquad [1]$$

where α is the metallic glass's thermal diffusivity, c_v is its volumetric specific heat, T_{env} is the ambient temperature, $\tau_{\text{glue}} \approx 0.01E$ from both experimental data and molecular dynamics (MD) simulations, and $c_S = \sqrt{\mu/\rho}$ is the shear wave speed. For Zr-based metallic glasses, Eq. **1** gives $L_{\text{inc}} \sim 10$ nm. Therefore, if the glass layer is just 5–10 nm thick, shear localization will not be able to develop in the usual fashion. Extensive experimental characterization of shear bands in bulk metallic glasses indicates that they have a characteristic width of 10–50 nm (17, 19–21). This supports our notion that when the thickness of a metallic glass layer is below an intrinsic length scale parameter, L_{inc}, of the metallic glass, a different mechanical response may be expected (length scale effect in the plastic deformation of metallic glasses).

Judging from the lack of dislocation pileups near the ACIs and homogeneous flow behavior of the amorphous phase, we postulate that the interplay between nanocrystalline layers and the nanoscale metallic glass may be the main reason for large ductility enhancements in both phases. The large defect cluster that evolves out of the amorphous phase (embryonic shear band), which could eventually fail the whole amorphous material, may have been stopped by the nanocrystalline layers before it reaches maturity (18). Similarly, dislocation structures and geometric incompatibilities, which could localize in nanocrystalline grains and GBs (causing large stress concentrations and perpetuating themselves by jumping from grains to grains), may have been disrupted and dissolved by the amorphous layers. To test this hypothesis ("quarantine principle"), we have conducted MD simulations of 5/10 and 5/35 nanolaminate systems in tension, using a Cu/Zr interatomic potential developed by Duan *et al.* (31). Although such simulations are limited by the timescale accessible, they provide crucial atomistic details unavailable to experiments. Here, our MD simulations have yielded information about basic defect energetics and geometric insights supportive of some basic tenets of our hypothesis.

At the outset of the plastic deformation in our simulations, it was noticed that dislocations are nucleated from ACIs (often triggered by STZ activities in the metallic glass layers) or from GBs or ACI–GB intersections, gliding across the nanocrystal layer, and being absorbed at the opposite ACI (Fig. 3 *A* and *B*; for simplicity, the GBs are not shown). Our simulations have shown that ACIs clearly act as natural sinks of dislocations, absorbing the dislocation content in the nanocrystalline copper after plastic work has been accomplished (32). To characterize the atomic-scale physics occurring in the metallic glass when dislocations are absorbed, we quantitatively compute the atomistic inelastic strain (18) in reference to a configuration before dislocation activities (Fig. 3 *C* and *D*; the atoms with the inelastic strains $<6\%$ are not shown). The STZs in the amorphous Cu/Zr layers can be clearly visualized as clusters of structurally disordered atoms. As the deformation starts, a few STZs can be seen to be activated in an uncorrelated fashion inside amorphous layers. Afterward, Shockley partials were nucleated from ACI and propagated inside the crystal, leaving behind the stacking faults. When a dislocation hit the opposite ACI, more STZs are activated in a correlated fashion near the intersection line between the dislocation slip plane and ACI (Fig. 3*C*). Subsequently they trigger other STZs nearby, and the entire inelastically deformed zone "diffuses" gradually into the deeper amorphous region. Another process that frequently accompanies dislocation absorption is ACI sliding (similar to GB sliding), which spreads the dislocation core along the ACI (33). ACI sliding occurs between crystalline and amorphous halves and shows up as small rafts of ordered atoms in Fig. 3*D* (highlighted with dashed circles). These atoms belong to the adjacent crystal plane oriented parallel to the ACI. The ACI has random structural variations because of the amorphous phase, leading to interfacial regions with weak shear strengths that are susceptible to sliding. The conversion of dislocation cores (geometric incompatibilities) into STZs and ACI sliding blunt the stress concentrations associated with the dislocation flux and homogenize the plastic flow of nanolaminates.

The behavior we observe is very different from those we have seen so far in crystalline–crystalline nanolaminates and single-phase nanocrystalline materials, where high stress concentrations are often encountered near dislocation pileups or GB triple junctions (34). It is not surprising that ACIs have very different inelastic shear (slip) transfer properties from those of GBs, because they belong to a different structural class of internal interfaces. GBs have 5 df (3 df for misorientation and 2 df for inclination), but ACIs have only 2 df (inclination, but no misorientation). Our atomistic simulations have revealed some unique features of shear/slip transfer

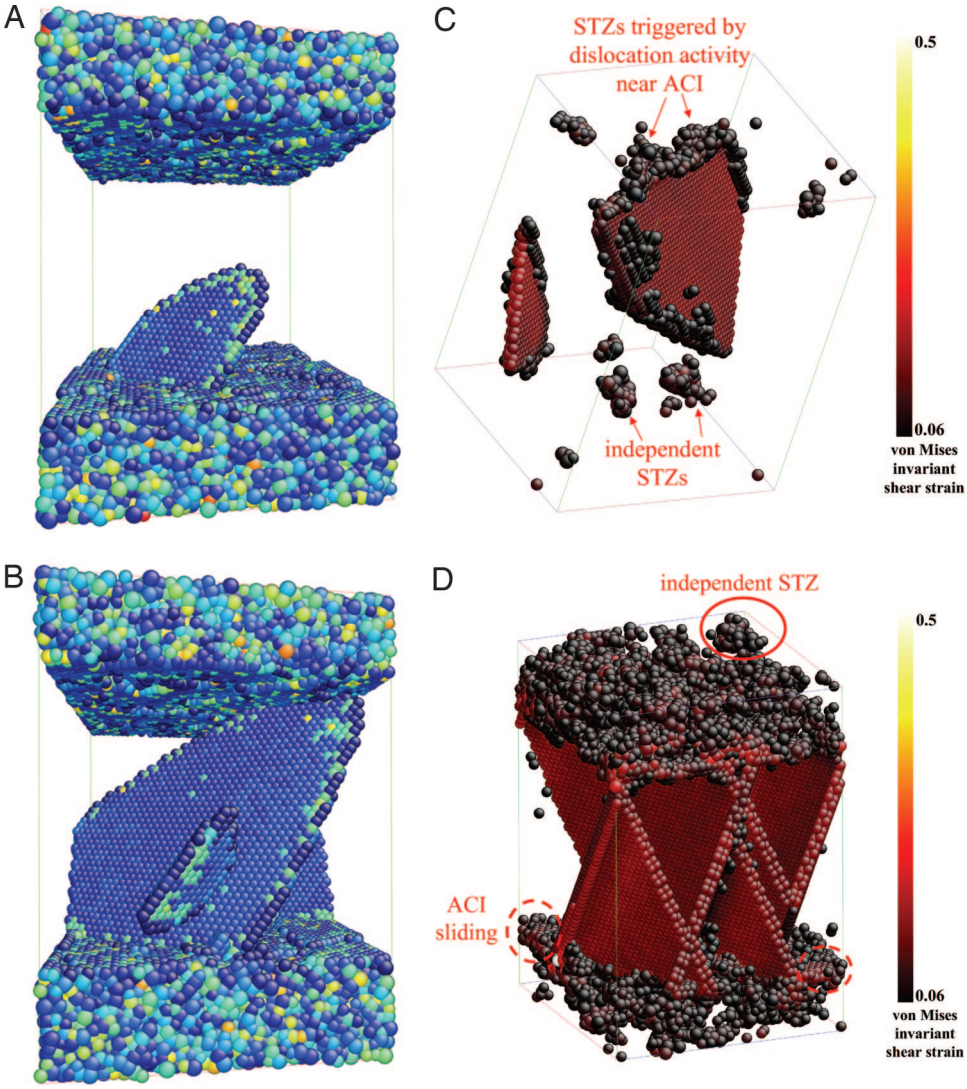

Fig. 3. MD simulations of 5/10 Cu/Zr system (10 × 15 × 10 nm, 105,336 atoms) under periodic boundary conditions. (*A*) Dislocation nucleates at the bottom ACI. The central symmetry parameter, which characterizes the degree of inversion symmetry breaking around each atom, is used to visualize the stacking fault, bounded by a Shockley partial dislocation. (*B*) Dislocation is absorbed by the amorphous layer at the top ACI. Simultaneously, another stacking fault system is activated and intersects the first stacking fault in the middle, forming a sessile dislocation junction. (*C*) Activation of STZs when the partial dislocation hits the amorphous layer. Atoms with inelastic strain below the strain threshold are not shown. STZs in the amorphous layers are clearly visible as clusters of inelastically transformed atoms. One also sees STZs forming spontaneously inside the amorphous layer at the bottom of the image. (*D*) Distribution of inelastic shear strain after dislocation absorptions, in reference to a configuration before dislocation activities. ACI sliding (similar to GB sliding) shows up on the lower right and upper left corners of the bottom ACI.

near ACIs compared with near GBs or crystalline–crystalline interfaces (CCIs). Near a GB or a CCI, slip/shear transfer happens by either core spreading along the shear-weak interface (35) or triggering of new slips in the companion grain but only at very limited selections of Burgers vectors and slip planes. Thus, large incompatibility and stress concentration could build up inside or near the GB or CCI during deformation. For problems like fracture, e.g., microcrack initiation by GB decohesion, one has to look at the extreme statistics, i.e., the worst case scenarios. In a nanocrystal with random grains, for example, one inevitably has two extremely misaligned grains (totally misaligned slip planes and high Schmid factor in one grain but low Schmid factor in another), where large geometric incompatibilities in the form of GB dislocations or lattice dislocation pileups could arise. This may be a key reason why some nanocrystalline materials show little tensile elongation to failure despite the observed enhanced strain rate sensitivity (36, 37). Such "extreme incompatibility" scenario will not nearly often arise at the ACIs, because the STZs in the amorphous materials are omnidirectional; e.g., there are infinite selections of possible inelastic shear modes to transfer to. For an incoming lattice dislocation, if slip transfer does not work out at one spatial point, it could still carry through at another spatial point down the line of intersection. In contrast, for a lattice dislocation impinging a CCI, if slip transfer does not go through at one point, it is likely that the entire line is stuck because of structural periodicity. From our large-scale MD simulations, we observed that slip transfer at ACIs is more ad hoc, diffuse, and efficient in removing the extreme grievances in the sense of extreme statistics. Less geometric incompatibility concentrated at ACIs means delayed decohesion and fracture initiation. The model also suggests that the enhanced m measured in our experiments arises most likely from ACI-based mechanisms, e.g., interactions of dislocations with amorphous layers as projected from the experimental observations of deformed nanocrystalline–amorphous nanolaminates.

The MD results indicate that the amorphous layers can significantly impact dislocation structures formed in the nanocrystalline layers (illustrated for the 5/35 system in Fig. 4). In the simulations, a great burst of dislocations is nucleated at the beginning of tensile deformation in both 5/10 and 5/35 systems, resulting in dense sessile dislocation forests (Fig. 4*A*). The rod-like sessile dislocations come from intersections of two nonparallel stacking faults or twinning systems (Fig. 3*B*, middle of crystal layer). As the simulation time progresses, however, the dislocation density decreases dramatically (Fig. 4*B*) because of the attraction and annihilation of dislocations in the metallic glass layers. This attraction destabilizes dislocation structures near ACIs. We find that not only the mobile dislocation segments but also the existing sessile dislocations are effectively drawn into the amorphous layers because of reactions with new mobile dislocations. Most of the dislocations we see in the simulations

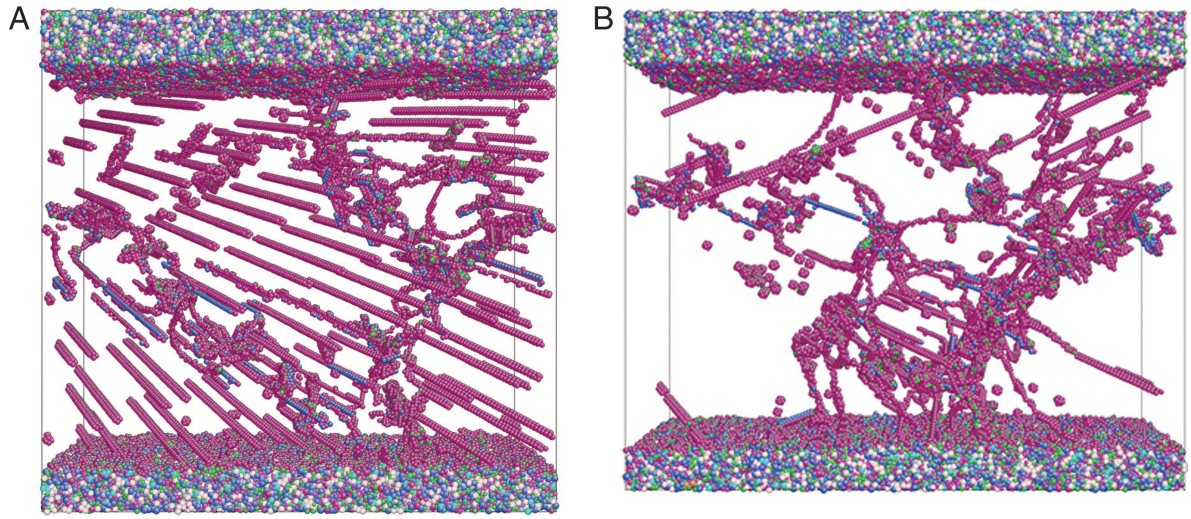

Fig. 4. Influence on dislocation structures by the presence of the amorphous phase, shown by $T = 300$ K MD simulations in the 5/35 Cu/Zr system ($37 \times 40 \times 8$ nm, 790,894 atoms). Atoms are color-coded by their coordination numbers [red, 11; blue, 13; green, 10; tan, 14; perfectly coordinated atoms (12) are not shown]. (*A*) A great burst of dislocation activities is induced initially by tension at the onset of yielding in the simulations, resulting in a dense sessile dislocation forest. (*B*) As simulation time progresses, the dislocation density decreases dramatically (after 11% additional strain with respect to *A*), indicating that the dislocation structures are drawn into the amorphous layers.

are single Shockley partial dislocations with associated stacking faults.

We emphasize the critical importance of dislocation slip mechanisms modulated by nanoscale metallic glass in sustaining the good ductility of our samples. The tensile tests of 5/5 samples revealed a high tensile strength of 1.96 GPa but a near-zero tensile elongation to failure, preempting any dislocation activities and plasticity. TEM showed penetration of the amorphous glassy $Cu_{\approx 3}Zr$ through the thickness of the crystal layers that resulted in drastic decrease of the tensile elongation. Our experimental results here also suggest that excessive storage of dislocations or pileups may not necessarily be the best avenue to achieve large tensile ductility in ultrahigh-strength materials. The high stress concentrations rendered from the dislocation pileups may very well promote GB voids/cracks and lead to early failure of nanocrystalline materials (23, 36). An optimal, intermediate level of dislocation or stacking fault storage is likely favorable for maximizing the ductility of nanostructured materials. Our experimental observations and simulations demonstrate that the nanoscale metallic glass layer not only sustains large tensile plasticity itself but is also likely to play the dominant mechanistic role, exhibiting an extraordinary capacity to act as both a dislocation source and sink to mediate inelastic shear/slip transfer while avoiding extreme stress concentrations that lead to fracture initiation. As such, it drastically enhances the tensile ductility of the entire crystalline–amorphous nanolaminates. The synergy between the nanoscale metallic glass and nanocrystalline layers in modulating dislocation behavior, enabled by the precise dimensional and chemistry control available with magnetron sputtering, is the feature that underlies the unusual mechanical properties of these nanolaminates.

The large tensile ductility and nearly ideal plastic flow behavior presented here suggest that the nanocrystalline–metallic glass composite approach is a viable route toward developing materials with mechanical performance beyond those achievable from single-phase elemental materials and vastly superior to those predicted from the simple rule-of-mixtures. Our results indicate that nanometer-sized metallic glasses can be used to enhance the very limited tensile ductility of nanocrystalline materials. The near-perfect elastoplasticity without any strain hardening has implications for room-temperature forming of nanoscale metallic glasses and crystalline–amorphous nanocomposites. We note that the solid-state amorphization process occurs in a number of material systems, such as Cu/Ti, Ni/Ti, Cu/Hf, Ag/Zr, Ni/Zr, Ag/Hf, Ni/Nb, Ti/Si, and Pd/Si. Therefore, the crystalline–amorphous nanolaminate approach is likely applicable to many other materials systems. This study provides impetus for future experimental and theoretical endeavors to predict, design, and explore such hybrid nanomaterial properties that are not readily available through conventional approaches (38).

Materials and Methods

The nanocrystalline–amorphous nanolaminate foils (up to 25 cm in diameter) were fabricated by using dc magnetron sputtering with alternating layers of high-purity Cu (99.999%) and Zr (99.7%) (39, 40). By controlling the thickness of each deposition layer, different variations of nanocrystalline Cu and amorphous Cu/Zr nanolaminates can be fabricated. For description purposes, we use sample notation, such as 5/35, which refers to the samples with 5-nm-thick Cu/Zr amorphous layers and 35-nm-thick nanocrystalline Cu layers. Because the grain size in the crystal layers equals approximately to the layer thickness, we were able to control the smallest grain size down to 5 nm (i.e., 5/5 system). Such small grain-sized materials were previously only available in computer simulations (7). For the 5/35 system, the deposited thicknesses of the Cu layer and Zr layer are 38.8 nm and 2.5 nm, respectively. Solid-state amorphization resulted in the formation of a 35-nm Cu layer and 5-nm amorphous Cu/Zr. Conservation of mass analysis indicated that the composition of the amorphous layer is $\approx Cu_3Zr$. Electron dispersive x-ray analysis supports this result. The samples we have fabricated typically include 5- to 10-nm-thick Cu/Zr amorphous layers, and 5- to 70-nm-thick nanocrystalline Cu layers.

The overall thickness of the as-fabricated samples was in the range of 20–110 μm. The initial Cu/Zr foils were deposited onto (100)Si wafers by using an argon working pressure of 3 mtorr (1 torr = 133 Pa). X-ray diffraction scans indicate that the nanocrystalline Cu layer has (111) out-of-plane texture and random in-plane orientations. The residual stresses of the as-deposited nanolaminates are typically small, in the range of ± 15 MPa, as measured by a FLX-2320 thin film stress measurement instrument (Tencor, San Jose, CA).

To prepare the dog-bone tensile specimens (the gauge length and width were 6 and 3 mm, respectively; previously reported tensile

tests of nanostructured metals typically used a gauge length in the range of 1–5 mm), two stainless steel plates (≈3 mm thick each) were first machined into the required sample geometry and used as dies [see supporting information (SI) Fig. 5]; then, Cu/Zr nanolaminate foils were sandwiched between these two plates and mechanically cut into the sample shape with a scalpel. Ethanol was used as the lubricant during the cutting, and the whole process did not involve grinding or thermal heating. The accurate dimensions of all samples were measured with a Axioplan2 optical microscope (Zeiss, Oberkochen, Germany) at a magnification of ×25, and the thickness was measured with a S-4500 scanning electron microscope (Hitachi, Tokyo, Japan). Experiments at Lawrence Livermore National Laboratory with samples prepared by electrodischarge machining and laser machining have demonstrated the local melting and crystallization of the amorphous $Cu_{\approx 3}Zr$ at the sample edges, resulting in a decreased tensile elongation to failure as reported in ref. 41. The uniaxial tensile tests were carried out in an Instron (Norwood, MA) 4444 tensile machine at a strain rate of 1×10^{-4} s^{-1}. The tensile elongation was measured by using an LE-01 laser extensometer (Electronic Instrument Research, Irwin, PA) having a displacement resolution of 1 μm. Two silver-colored tapes acting as reflective marks for tensile strain measurements were attached to the gauge surface of the samples.

The strain rate jump tests were performed in the same tensile machine in the strain rate range of 1×10^{-4} to 7×10^{-4} s^{-1}. The strain rate sensitivity was calculated by using the standard formula

$$m = \left(\frac{\partial \ln \sigma}{\partial \ln \dot{\varepsilon}} \right)_{T,\varepsilon}$$

where σ and $\dot{\varepsilon}$ are the flow stress and the strain rate, respectively. TEM was performed on a CM300-FEG microscope (Philips, Eindhoven, The Netherlands) operated at 300 kV. The cross-sectional and plan-view TEM samples were prepared by using dual focus ion beam technique and double jet electropolishing, respectively. The microstructures of the nanolaminates were found to be uniform throughout the thickness regardless the total thickness of the samples.

The room-temperature cold rolling experiments were carried out at the strain rate of $\approx 10^0$ s^{-1}. The foils were sandwiched between two polished stainless steel plates between each rolling pass. The degree of the deformation is defined by using the percentage of thickness reduction as $(h_0 - h)/h_0 \times 100\%$, where h_0 and h are the thickness of the samples or individual layers before and after rolling. Our TEM observations indicate that despite the large rolling strain (50% thickness reduction), the layer structure of nanolaminates remains intact, and the plastic flow of the amorphous metallic glass layer was found homogeneous. To record the thickness reduction of amorphous and nanocrystalline layers during tensile tests and rolling experiments, we have measured the overall sample thickness reduction, bilayer thickness reduction (crystalline plus amorphous layers), as well as the individual amorphous layer thickness reduction in TEM. These measurements yield rather consistent results in a way such that the thickness reduction of the amorphous layers can be systemically documented. The result shown in Fig. 2*E* is an example of how the measurements were performed. We call it "local strain" because of the wavy nature of the ACIs.

The reference Cu/304 stainless steel (304 SS) crystalline nanolaminate samples were fabricated by using sputter deposition. The mechanical property measurements on these samples with different bilayer thickness indicate that, when the bilayer thickness is <100 nm, the tensile elongation to failure of Cu/304 SS nanolaminates falls in the range of 1–4%, which is substantially less than that seen in Cu/Zr nanocrystalline–amorphous nanolaminates.

Simulation Details. We adopt the Cu–Zr interatomic potential of Duan *et al.* (31). The nanocrystalline–amorphous multilayer configuration is produced from a reference solid structure (single-crystal or polycrystal) of pure Cu by (*i*) random replacements of Cu with Zr in selected slices; (*ii*) melting of the selected slices by keeping the temperature at 1,600 K while constraining the rest of the atoms to be immobile; (*iii*) slow quench of the selected slices to 650 K, where the Cu–Zr layer undergoes glass transition at ≈700 K; (*iv*) slow quench of the entire system (the rest of the atoms no longer constrained) from 650 to 300 K. During simulations, uniaxial tension is applied in $\langle 11\bar{2} \rangle$ direction, with strain rate of $\approx 1 \times 10^8$ s^{-1}. Periodic boundary conditions are applied in all three dimensions. The inelastic or transformation strain was calculated and rendered atom by atom. The atoms with the inelastic strain <6% are not shown in Fig. 3 *C* and *D*. We also observed ACI sliding (akin to GB sliding) triggered by dislocation absorption. Additional MD simulation setup and results can be seen in *SI Text*, SI Figs. 6–8, and SI Movies 1–3.

We thank Prof. W.D. Nix for careful reading of this manuscript; M. Wall, P. Ramsey, and J. Chesser for experimental assistance; and the user facility of the National Center for Electron Microscopy, Lawrence Berkeley Laboratory. This work was performed under the auspices of the U.S. Department of Energy by the University of California, Lawrence Livermore National Laboratory, under Contract W-7405-ENG-48. Y.W. was partially supported by National Science Foundation Grant CMMI-0653769. J.L. was supported by National Science Foundation Grant DMR-0502711, Office of Naval Research Grant N00014-05-1-0504, the Air Force Office of Scientific Research, the Department of Energy, and the Ohio Supercomputer Center.

1. Schall P, Cohen I, Weitz DA, Spaepen F (2006) *Nature* 440:319–323.
2. Ovid'ko IA (2002) *Science* 295:2386.
3. Ogata S, Li J, Yip S (2002) *Science* 298:807–811.
4. Nix WD (1998) *Scr Mater* 39:545–554.
5. Champion Y, Langlois C, Guerin-Mailly S, Langlois P, Bonnentien JL, Hytch MJ (2003) *Science* 300:310–311.
6. Weertman JR (2004) *MRS Bull* 29:616–620.
7. Schiøtz J, Jacobsen KW (2003) *Science* 301:1357–1359.
8. Huang HB, Spaepen F (2000) *Acta Mater* 48:3261–3269.
9. Mara N, Sergueeva A, Misra A, Mukherjee AK (2004) *Scr Mater* 50:803–806.
10. Misra A, Zhang X, Hammon D, Hoagland RG (2005) *Acta Mater* 53:221–226.
11. He G, Eckert J, Loser W, Schultz L (2003) *Nat Mater* 2:33–37.
12. Inoue A, Zhang W, Tsurui T, Yavari AR, Greer AL (2005) *Philos Mag Lett* 85:221–229.
13. Xu D, Lohwongwatana B, Duan G, Johnson WL, Garland C (2004) *Acta Mater* 52:2621–2624.
14. Zhang Y, Wang WH, Greer AL (2006) *Nat Mater* 5:857–860.
15. Sheng HW, Luo WK, Alamgir FM, Bai JM, Ma E (2006) *Nature* 439:419–425.
16. Argon AS (1979) *Acta Metall* 27:47–58.
17. Zhang Y, Greer AL (2006) *Appl Phys Lett* 89:071907.
18. Shimizu F, Ogata S, Li J (2006) *Acta Mater* 54:4293–4298.
19. Li J, Spaepen F, Hufnagel TC (2002) *Philos Mag A* 82:2623–2630.
20. Pekarskaya E, Kim CP, Johnson WL (2001) *J Mater Res* 16:2513–2518.
21. Vaidyanathan R, Dao M, Ravichandran G, Suresh S (2001) *Acta Mater* 49:3781–3789.
22. Balk TJ, Dehm G, Arzt E (2003) *Acta Mater* 51:4471–4485.
23. Wang YM, Wang K, Dan P, Lu K, Hemer KJ, Ma E (2003) *Scr Mater* 48:1581–1586.
24. Lu L, Shen YF, Chen XH, Qian LH, Lu K (2004) *Science* 304:422–426.
25. Youssef KM, Scattergood RO, Murty KL, Horton JA, Koch CC *Appl Phys Lett* 87:091904, 2005.
26. McFadden X, Mishra RS, Valiev RZ, Zhilyaev AP, Mukherjee AK (1999) *Nature* 398:684–686.
27. McClintock FA, Argon AS (1966) in *Mechanical Behavior of Materials* (Addison–Wesley, Reading, MA), pp 320–322.
28. Hutchinson JW, Neale KW (1977) *Acta Met* 25:839–846.
29. Wang YM, Ma E (2004) *Acta Mater* 52:1699–1709.
30. Chen J, Lu L, Lu K (2006) *Scr Mater* 54:1913–1918.
31. Duan G, Xu DH, Zhang Q, Zhang GY, Cagin T, Johnson WL, Goddard WA (2005) *Phys Rev B* 71:224208.
32. Rodney D, Deby JB, Verdier M (2005) *Modelling Simul Mater Sci Eng* 13:427–436.
33. Gao HJ, Zhang L, Baker SP (2002) *J Mech Phys Solids* 50:2169–2202.
34. Ovid'ko IA, Sheinerman AG (2004) *Acta Mater* 52:1201–1209.
35. Hoagland RG, Hirth JP, Misra A (2006) *Philos Mag* 86:3537–3558.
36. Wang YM, Hamza AV, Ma E (2006) *Acta Mater* 54:2715–2726.
37. Zhu T, Li J, Samanta A, Kim HG, Suresh S (2007) *Proc Natl Acad Sci USA* 104:3031–3036.
38. Ashby MF, Brechet YJM (2003) *Acta Mater* 51:5801–5821.
39. Weihs TP, Barbee TW, Jr, Walls MA (1997) *Acta Mater* 45:2307–2315.
40. Barbee TW, Jr (1985) in *Synthetic Modulated Structures*, ed Chang L, Giessen BC (Academic, New York), pp 313–317.
41. Nieh TG, Barbee TW, Jr, Wadsworth J (1999) *Scr Mater* 41:929–935.